Journal of Engineering and Technology for Industrial Applications

ISSN ONLINE:

ITEGAM-JETIA

Manaus, v.12 n.58, p. 87-97. March/April, 2026.
DOI: https://doi.org/10.5935/jetia. v12i58.2888

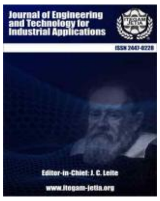

RESEARCH ARTICLE **OPEN ACCESS**

ANFIS-BASED MPPT STRATEGY FOR SOLAR WATER PUMPING SYSTEM

Islam Hachemi*[1], Kamel Haddouche[2], Ahmed Bouzidane[3] and Mustapha Belarbi[4]

[1, 2, 3]Research Laboratory of Industrial Technologies, Faculty of Applied Sciences, University of Tiaret, B. P. 78 - 14000 Tiaret, Algeria.
[4]Energy Engineering and Computer Engineering Laboratory, Faculty of Applied Sciences, University of Tiaret, B. P. 78 - 14000 Tiaret, Algeria.

[1]https://orcid.org/0009-0001-5487-0648, [2]https://orcid.org/0000-0002-7084-0246,
[3]https://orcid.org/0009-0001-9731-1870, [4]https://orcid.org/0000-0002-0614-9944

Email: *hachemi.islam1414@gmail.com, haddouchekam@gmail.com, ahmed.bouzidane@gmail.com, mustapha_belarbi@univ-tiaret.dz

ARTICLE INFO

Article History
Received: November 4, 2025
Reviewed: January 15, 2026
Accepted: January 7, 2026
Published: March 31, 2026

Keywords:
PV water pumping system,
ML techniques,
Squirrel-cage motor,
Centrifugal pump,
MPPT,
PI controller.

ABSTRACT

This paper presents the modeling and control of a standalone solar water pumping system, comprising a PV generator, DC/AC inverter, squirrel-cage motor, centrifugal pump, hydraulic circuit, and MPPT controller. Four machine-learning techniques (ANN, ANFIS, SVM, and GPR) are assessed for predicting the MPP voltage to improve system efficiency. Comparative results show that ANFIS gives the highest prediction accuracy ($R^2 = 0.9992$ and $RMSE = 0.9552$), outperforming GPR and ANN, with SVM providing moderate performance during training and testing phases. The performance of predcitive models was evaluated using training and testing data, assessing accuracy in predicting optimal voltage based on irradiance and temperature. Dynamic simulations under step-change irradiance conditions confirmed that the ML-based MPPT controllers significantly outperformed conventional P&O and INC methods, achieving faster time response. Based on this analysis, an ANFIS-based MPPT strategy with a PI controller is used, leveraging its superior accuracy relatively to the other ML-based MPPT controllers and conventional methods (P&O and INC).

I. INTRODUCTION

In solar water pumping systems, PV generator performance is affected by varying environmental conditions and load characteristics. MPPT techniques mitigate these challenges by maximizing power extraction under these condition. While numerous MPPT exist, the Perturb and Observe (P&O) and Incremental Conductance (INC) methods are most prevalent due to their simplicity [1]. The use of artificial intelligence (AI) techniques has proliferated across diverse research disciplines and industrial sectors in recent years [2]. These techniques can be applied to tackle the challenges of MPPT in PV systems. For this purpose, researchers in [3] introduced a novel hybrid model that enhances the ANFIS model by integrating the BAT algorithm for training.

The results indicate that this metaheuristic approach offers superior training efficiency compared to conventional backpropagation algorithm. Similarly, a hybrid algorithm was proposed in [4], employing the Crowded Plant Height Optimization algorithm for ANFIS training resulted in improved tracking speed and efficiency relative to a standard ANFIS. In [5], the authors present an SVM model for predicting photovoltaic energy production by using solar irradiance and ambient temperature as inputs. While achieving a low MAPE, the model demonstrated sensitivity to input data errors. Similarly, another method involving SVM technique is presented in [6] by using three input combinations based on temperature and irradiance.

While achieving a MAPE of 36 %, outperforming analytical methods, the model exhibited sensitivity to climate variability. In [7], a PV power system (PVPS) topology is introduced by incorporating a radial basis function neural network (RBFNN) to enhance system efficiency; the results demonstrated the superiority of this MPPT method over conventional techniques. In [8], researchers have developed and implemented soft computing (SC) based MPPT controllers to predict optimal converter duty cycles under varying climatic conditions and static heads. A comparative study was conducted to assess and validate the accuracy. Authors in [9] applied the Golden Section Search (GSS) algorithm as an MPPT technique to enhance the efficiency of a standalone PV water pumping system (PVWPS).

Matlab/Simulink simulations verified the effectiveness of this approach. In [10], several ANN-based methods are presented for predicting hourly water flow rates in a PVWPS; their findings demonstrated accurate predictions based on measured air temperature and solar irradiation. The present work concerns the modeling and control of a standalone solar water pumping system. In addition, a comparative analysis between four ML techniques (ANN, ANFIS, SVM, and GPR) is presented for predicting the voltage at the MPP of the PV generator. This paper is organized into four sections. Section II describes the mathematical formulations used for the various components of the investigated PVWPS. The simulation results are reported and discussed in Section III. Finally, Section IV summarizes the findings and conclusions.

II. MATHEMATICAL MODELING

The proposed PVWPS integrates various components; such as: PV generator, DC/AC inverter, squirrel-cage induction motor, centrifugal pump, hydraulic circuit, and MPPT controller.

II.1 PV GENERATOR

Numerous mathematical models exist to describe the nonlinear behavior of the solar cell in PV module, differing in complexity and the number of parameters used to calculate voltage and current. This study utilizes the one-diode model, whose equivalent circuit is shown in Figure 1.

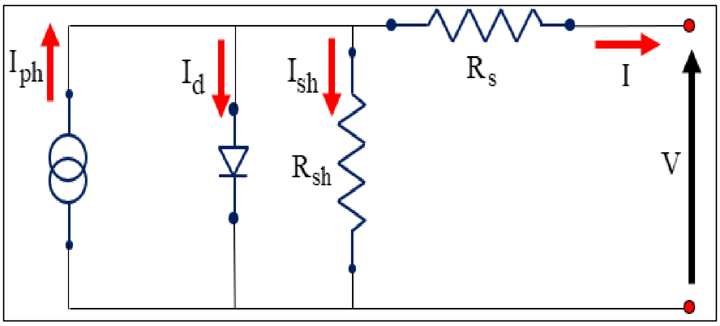

Figure 1: Equivalent circuit of the one-diode model of the cell.
Source: Authors, (2026).

Notice that the single-diode model is simpler with five unknown parameters (R_s, R_{sh}, A, I_0, I_{ph}). It may not capture the complexities of the cell behavior as accurately as the double-diode model, particularly under diverse operating conditions. Its simplicity, efficiency, and sufficient accuracy make it suitable for many systems design applications. By applying Kirchhoff's current law, the output current of a solar cell can be mathematically represented as follows:

$$I = I_{ph} - I_d - I_{sh} \tag{1}$$

Where I_{ph}, I_d and I_{sh} represents respectively the photocurrent, the diode current, and the current leak in the shunt resistor. The photocurrent is defined by:

$$I_{ph} = \frac{G}{G_{ref}}\left(I_{ph\_ref} + \mu_{sc}\cdot\left(T_c - T_{c\_ref}\right)\right) \tag{2}$$

With G is the solar radiation intensity, G_{ref} is the solar radiation intensity at STC, I_{ph_ref} is the photocurrent at STC, T_{c_ref} is the cell temperature at STC, T_c is the cell temperature, and μ_{sc} is the coefficient temperature of short-circuit current. The diode current is given by Shockley’s diode equation as follows:

$$I_d = I_0 \cdot \left(e^{\frac{q\cdot(V+R_s\cdot I)}{A\cdot K\cdot T}} - 1\right) \tag{3}$$

I_0 represents the reverse saturation current of the diode, q is the electron charge, R_s is the series resistance, V and I represent respectively the PV module operation voltage and current, k is the Boltzmann’s constant, and A is the diode ideality factor. The current leak in the shunt resistor can be computed by the following equation:

$$I_{sh} = \frac{V + R_s \cdot I}{R_{sh}} \tag{4}$$

Where R_{sh} is the shunt resistance. The overall output current and voltage of the generator are given by:

$$\begin{cases} I_{gen} = N_p \cdot I \\ V_{gen} = N_s \cdot V \end{cases} \tag{5}$$

Where N_p and N_s are respectively the number of the PV modules interconnected in series and/or parallel configurations.

II.2 DC/AC INVERTER

The DC/AC inverter converts the direct current (DC) voltage generated by the solar array into a variable-frequency three-phase alternating current (AC) voltage. The three-phase inverter output voltages are calculated using the following equation:

$$\begin{bmatrix} V_a \\ V_b \\ V_c \end{bmatrix} = \frac{V_{DC}}{3} \begin{bmatrix} 2 & -1 & -1 \\ -1 & 2 & -1 \\ -1 & -1 & 2 \end{bmatrix} \cdot \begin{bmatrix} S_1 \\ S_2 \\ S_3 \end{bmatrix} \tag{6}$$

S_i is the state of the IGBT switch.

II.3 SQUIRREL-CAGE INDUCTION MOTOR

Employing the Park’s transformation, the three-phase squirrel-cage induction motor's voltage is calculated in the d-q reference frame using the following equation:

$$\begin{cases} \begin{bmatrix} V_{ds} \\ V_{qs} \end{bmatrix} = R_s \begin{bmatrix} I_{ds} \\ I_{qs} \end{bmatrix} + \dfrac{d}{dx} \begin{bmatrix} \varphi_{ds} \\ \varphi_{qs} \end{bmatrix} + \omega_s \begin{bmatrix} 1 & 0 \\ 0 & 1 \end{bmatrix} \begin{bmatrix} \varphi_{ds} \\ \varphi_{qs} \end{bmatrix} \\ \begin{bmatrix} V_{dr} \\ V_{qr} \end{bmatrix} = R_r \begin{bmatrix} I_{dr} \\ I_{qr} \end{bmatrix} + \dfrac{d}{dx} \begin{bmatrix} \varphi_{dr} \\ \varphi_{qr} \end{bmatrix} + \omega_r \begin{bmatrix} 1 & 0 \\ 0 & 1 \end{bmatrix} \begin{bmatrix} \varphi_{dr} \\ \varphi_{qr} \end{bmatrix} \end{cases} \tag{7}$$

For the d-axis, V_{ds}, I_{ds}, φ_{ds}, V_{dr}, I_{dr} and φ_{dr} referred stator and rotor voltage, current and flux linkage, respectively. For the q-axis, the last variables are referred V_{qs}, I_{qs}, φ_{qs}, V_{dr}, I_{dr} and φ_{dr}. R_s and R_r are stator and rotor winding resistance. ω_s and ω_r are stotor and rotor frequency. For this study, V_{dr} and I_{dr} are set to zero. The d-q frame currents for the induction motor are given as follows:

$$\begin{cases} \begin{bmatrix} I_{ds} \\ I_{qs} \end{bmatrix} = \dfrac{L_r}{L_s \cdot L_r - M_{sr}^2} \begin{bmatrix} \varphi_{ds} \\ \varphi_{qs} \end{bmatrix} - \dfrac{M_{sr}^2}{L_s \cdot L_r - M_{sr}^2} \begin{bmatrix} \varphi_{dr} \\ \varphi_{qr} \end{bmatrix} \\ \begin{bmatrix} I_{dr} \\ I_{qr} \end{bmatrix} = \dfrac{L_r}{L_s \cdot L_r - M_{sr}^2} \begin{bmatrix} \varphi_{dr} \\ \varphi_{qr} \end{bmatrix} - \dfrac{M_{sr}^2}{L_s \cdot L_r - M_{sr}^2} \begin{bmatrix} \varphi_{ds} \\ \varphi_{qs} \end{bmatrix} \end{cases} \tag{8}$$

Where L_s, L_r and M_{sr} are respectively stator inductance, rotor inductance, and the mutual inductance. The electromagnetic torque is calculated as follows:

$$T_e = 1.5p \cdot M_{sr} \cdot \left(I_{qs} \cdot I_{dr} - I_{ds} \cdot I_{qr}\right) \tag{9}$$

Where p is the pair pole number. The motor speed is determined using the following mechanical dynamic equation:

$$T_e = \frac{J}{p} \cdot \frac{d\omega_r}{dt} + f \cdot \omega_r + T_r \tag{10}$$

Where T_r is the load torque, f is a viscous torque constant, J is the inertia moment of the rotor.

II.4 CENTRIFUGAL PUMP

The power required to pump water at a volumetric flow rate Q and total head H is calculated using the following equation:

$$P_h = g \cdot \rho \cdot H \cdot Q \tag{11}$$

The mechanical power consumed by the pump is defined by:

$$P_m = \frac{P_h}{\eta} = T_r \cdot \omega_r \tag{12}$$

Where g is the acceleration of gravity, ρ is the density of fluid (water), and η is the pump efficiency. Using equations (11) and (12), the load torque can be determined as follows:

$$T_r = \frac{g \cdot \rho \cdot H \cdot Q}{\omega_r \cdot \eta} \tag{13}$$

In general, pumps are described by their H(Q) characteristic that defines the total head as a function of flow rate for a single nominal speed (N_n); the equation that links the total head with the flow rate for any rotational speed (N) is given as follows:

$$H(Q, N^*) = h_0 \cdot (N^*)^2 - h_1 \cdot N^* \cdot Q - h_2 \cdot Q^2 \tag{14}$$

Where $N^* = \frac{N}{N_n}$ is the normalized speed. The load torque caused by flow through the hydraulic part of the pump takes a similar form to the total head equation, and can be written as:

$$T_r(Q,N^*) = c_0 \cdot (N^*)^2 - c_1 \cdot N^* \cdot Q - c_2 \cdot Q^2 \tag{15}$$

The coefficients h_0, h_1, h_2, c_0, c_1 and c_2 are calculated from the data provided by the manufacturer.

II.5 HYDRAULIC CIRCUIT

The pump must overcome the total head comprising static head, dynamic head, pipe friction losses, and components head losses.

$$HMT = H_s + H_d + H_{friction} + H_{components} \tag{16}$$

Pipe frictional losses can be calculated using the Darcy-Weisbach equation done by:

$$H_{friction} = \lambda \cdot \frac{L}{d} \cdot \frac{8 \cdot Q^2}{g \cdot \pi^2 \cdot d^4} \tag{17}$$

Where λ is the average friction factor, L is the length of the pipe, and d is the inside pipe diameter. Components head losses is given by:

$$H_{components} = \sum_{components} K_{component} \frac{8 \cdot Q^2}{g \cdot \pi^2 \cdot d^4} \tag{18}$$

Where K represents the fitting loss coefficient of each component. The total head is expressed by the following equation:

$$\mathrm{HMT} = \mathrm{H_s} + \mathrm{H_d} + \left(\lambda \cdot \frac{\mathrm{L}}{\mathrm{d}} + \mathrm{K}\right) \frac{8 \cdot \mathrm{Q}^2}{\mathrm{g} \cdot \pi^2 \cdot \mathrm{d}^4} \tag{19}$$

II.6 MPPT CONTROLLER

To enhance the energy efficiency of PV systems, it is essential to design an effective MPPT technique. Traditionally, the MPP has been tracked using conventional algorithms such as P&O and INC. The P&O method is widely used due to its simplicity; it works by slightly perturbing the operating voltage and observing changes in output power to approach the MPP. The INC algorithm is based on the slope of the power-voltage (P–V) curve, which equals zero at the MPP. While these classical techniques are effective under steady conditions, their performance often degrades under rapidly changing environmental conditions such as partial shading or sudden irradiance variations. To address these limitations, recent research has turned to machine-learning techniques.

By integrating AI into MPPT controllers, PVWPS can achieve faster convergence, improved accuracy, and better adaptability, making these techniques a promising direction for future advancements in solar energy technologies. For this purpose, a comparative analysis of ML techniques will be conducted in this study. The mathematical formulations of used ML techniques are reported in Appendix A. Notice, that the proposed control strategy is a two-parts system: the first part is an MPPT, which can be one of ML techniques (ANN, ANFIS, SVM or GPR) that uses irradiance and temprétaure as inputs for predicting the optimal PV generator voltage; the second part is a proportional-integral (PI) controller that regulates the generator terminal voltage to match the MPPT prediction, maintaining the V/f ratio.

III. RESULTS AND DISCUSSIONS

As can be seen in Figure 2, the proposed PVWPS is composed of PV modules type KC200GT, three-phase DC/AC inverter, a centrifugal pump driven by a 2.2 kw squirrel cage induction motor, hydraulic circuit, and MPPT. The system has been programmed under the Matlab/Simulink environment; the parameters used in the simulation are shown in Appendix B.

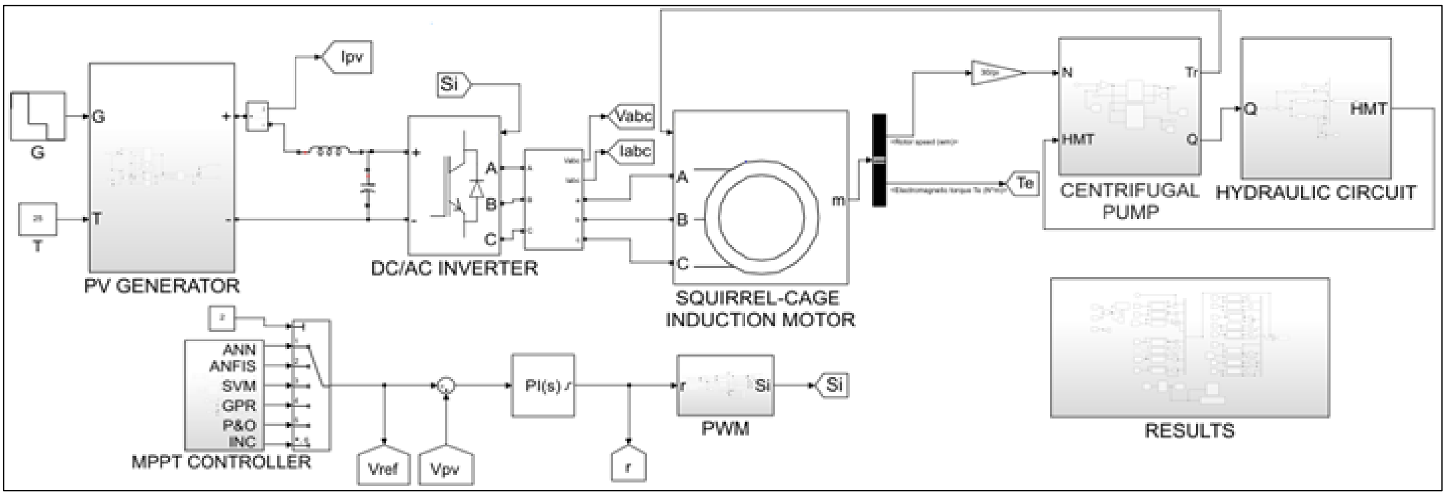

Figure 2: Design of the proposed PVWPS in Matlab/Simulink.
Source: Authors, (2026).

III.1 COMPARATIVE ANALYSIS OF ML TECHNIQUES

In this part, a comparative analysis of ML techniques (ANN, ANFIS, SVM, and GPR) is performed to predict the optimal voltage used as a reference signal for the PI controller. The observed data is derived through a numerical compilation based on measurements provided by the manufacturer. The inputs of the predictive models are irradiance and ambient temperature. The dataset is segregated into two subsets: training and testing. Notice, that 70 % of the dataset is used for the training, with the remainder utilized for the testing phase. The developed ANN employs a multilayer feed-forward with a 2-3-1 structure; the number of hidden neurons “3” was selected via different simulations to maximize R and minimize RMSE. For ANFIS, a “4 3” structure was implemented by using Gaussian membership function for the inputs, with a grid partition and hybrid learning method limited to a maximum of 30 epochs.

The SVM model used a quadratic kernel function, selected from a range of six tested kernels within Matlab. The selected GPR technique employed a Matern 5/2 kernel function. This last was selected from a range of tested kernels, including Rational Quadratic, Squared Exponential, and Exponential. Default settings were adopted for the hyperparameters of both SVM and GPR. The training of these techniques is performed offline based on weather conditions. During simulation, the ML-MPPT receives the input information and provides predictions instantaneously, which is analogous to a testing phase. The simulation outcomes obtained during the training and testing phases using ANN, ANFIS, SVM, and GPR are presented in Tables 1 and 2.

Table 1: Comparison between the observed and predicted values.

Data	**Inputs**		**Observed V_{MPP} (V)**	**Predicted V_{MPP} (V)**			
	T (°C)	**G (kW/m^2)**		**ANN**	**ANFIS**	**SVM**	**GPR**
Training	20	1	382.34	381.69	382.06	385.98	381.99
	20	0.6	414.54	416.28	414.53	413.91	415.67
	20	0.4	428.40	427.52	429.03	424.74	427.95
	25	1	368.48	369.37	369.27	371.89	369.11
	25	0.8	386.96	386.29	386.47	386.77	386.58
	25	0.4	414.54	413.68	414.05	410.27	413.52
	25	0.2	419.16	418.20	418.63	418.89	418.41
	30	0.8	373.10	371.92	372.47	372.63	372.41
	30	0.6	386.96	387.89	388.06	385.30	387.57
	30	0.2	400.68	402.96	400.93	404.36	402.40
	35	1	340.90	341.48	340.86	343.94	341.04
	35	0.6	373.10	372.31	372.04	371.11	372.32
	35	0.4	382.34	382.93	382.77	381.55	382.82
	40	1	327.04	326.86	326.66	330.08	326.49
	40	0.8	340.90	341.42	341.82	344.58	341.93
	40	0.4	368.48	367.49	368.22	367.31	367.99
	40	0.2	373.10	372.25	373.14	375.54	372.70
	50	0.8	313.18	312.66	313.15	316.84	313.14
	50	0.6	327.04	328.21	327.21	328.99	327.79
	50	0.4	340.90	340.02	340.39	339.06	339.80
	50	0.2	345.38	346.12	345.73	347.03	345.88
Testing	20	0.8	400.68	399.36	398.84	400.99	399.65
	20	0.2	433.02	432.34	434.88	433.49	433.82
	25	0.6	400.68	402.74	402.15	399.57	402.16
	30	1	354.62	355.82	354.98	357.88	355.39
	30	0.4	396.06	398.59	397.53	395.87	398.16
	35	0.8	354.62	356.75	357.22	358.57	357.33
	35	0.2	386.96	387.37	386.85	389.91	387.05
	40	0.6	354.62	356.73	355.90	356.99	356.94
	50	1	299.32	298.88	298.14	302.60	299.13

Source: Authors, (2026).

To evaluate the performance of predictive models, R-squared and RMSE between observed and predicted values are used. The mathematical formulations of performance indicators are given as follows:

$$R^2 = 1 - \frac{\sum_{k=1}^{n} \left(V_{MPP\,obs}(k) - V_{MPP\,pred}(k)\right)^2}{\sum_{k=1}^{n} \left(V_{MPP\,obs}(k) - \bar{V}_{MPP\,obs}(k)\right)^2} \tag{20}$$

$$RMSE = \sqrt{\frac{\sum_{k=1}^{n} \left(V_{MPP\,obs}(k) - V_{MPP\,pred}(k)\right)^2}{n}} \quad (21)$$

Table 2 presents a comparative analysis of the performance indicators for the ML techniques.

Table 2: Performance indicators for the predictive models.

Phase	Indicator	ANN	ANFIS	SVM	GPR
Training	**RMSE**	0.9971	0.5472	2.5902	0.7613
	R-squared	0.9990	0.9997	0.9935	0.9994
Testing	**RMSE**	1.6206	1.5305	2.4242	1.5504
	R-squared	0.9981	0.9983	0.9957	0.9982
All data	**RMSE**	1.2181	0.9552	2.5415	1.0615
	R-squared	0.9987	0.9992	0.9943	0.9990

Source: Authors, (2026).

The results reveal that all models exhibit strong performance, characterized by high R-squared (0.9935 – 0.9997) and low RMSE (0.5472 – 2.5902). Notably, the ANFIS model demonstrates high accuracy during both training and testing. This is marked by relatively low RMSE values of 0.5472 and 1.5305, respectively, and high R-squared values of 0.9997 and 0.9983. Followed by GPR and ANN. The SVM model, although exhibiting reasonable performance during both training and testing. Considering the results across all data, the ANFIS technique demonstrates superior predictive accuracy with the lowest overall RMSE and higher R-squared. For this reason, the ANFIS technique is maintained for the simulation of the PVWPS. A comparison of the performances between the predictive models based on ML techniques and those using conventional algorithms is now presented in Figure 3. For this, step changes in irradiance level were applied at 2 s and 3 s. Irradiance level is changed from 0.6 kW/m^2 to 0.7 kW/m^2, then from 0.7 kW/m^2 to 0.5 kW/m^2, and then from 0.5 kW/m^2 to 0.4 kW/m$^{2.}$.

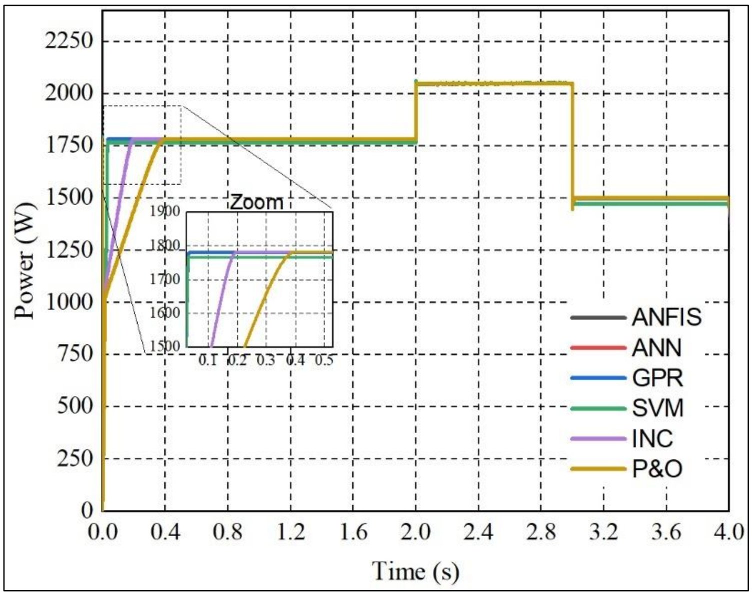

Figure 3: PV power for step change in irradiation level.
Source: Authors, (2026).

Figure 3 indicates that the ML techniques exhibit superior tracking performance compared to other conventional methods, as evidenced by faster rise time of 0.033 s in contrast to the 0.2 and 0.4 s rise time observed in INC and P&O methods, respectively. This is due to the significant impact of predicting V_{MPP} as opposed to calculating it directly.

III.2 ANFIS-BASED MPPT STRATEGY FOR THE PVWPS

In this part, the simulation results for step change in irradiance level condition are depicted in Figures 4 to 12. A multiple step change in irradiation level is applied. It went from 0.5 kW/m^2 to 0.6 kW/m^2 and then from 0.6 kW/m^2 to 0.4 kw/m^2. As depicted in the voltage profile (Figure 4), the ANFIS-based control strategy effectively maintains the PV generator operation near its MPP. The controller adjusts to each new irradiance level within a transient period of approximately 0.04 s. A consistent, slight decrease in the V_{MPP} is observed during irradiance drops, while an increase is seen during recovery. This minor variation is attributed to the negligible influence of irradiance on V_{MPP}.

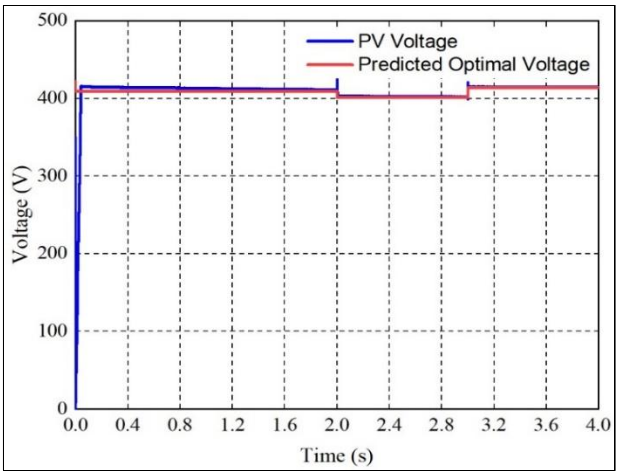

Figure 4: PV voltage and reference voltage.
Source: Authors, (2026).

Conversely, in Figure 5, the PV current exhibits significant sensitivity to irradiance changes. During irradiance increase, the current recovers proportionally, returning the PV generator to a higher power output. During irradiance decreases, the current drops substantially, leading to a proportional decrease in generated power. This is due to the direct correlation between irradiance and I_{sc}.

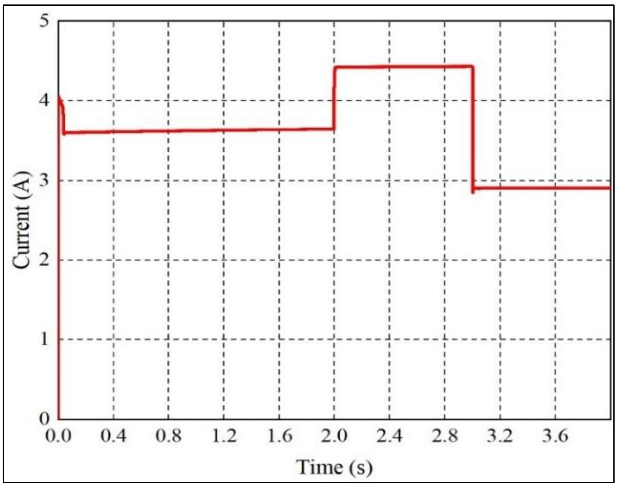

Figure 5: PV current.
Source: Authors, (2026).

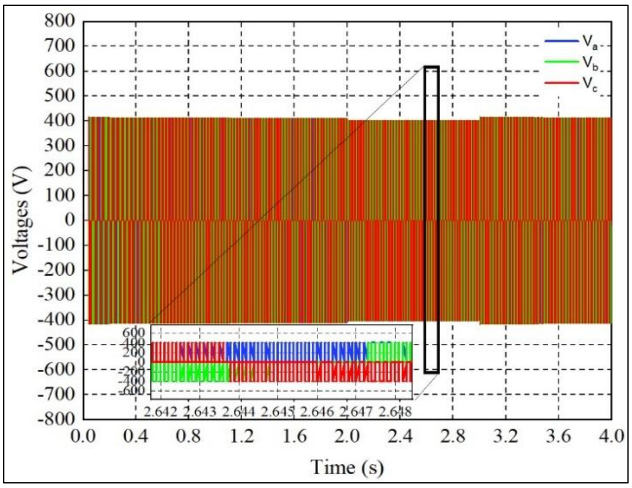

Figure 6: Line voltages.
Source: Authors, (2026).

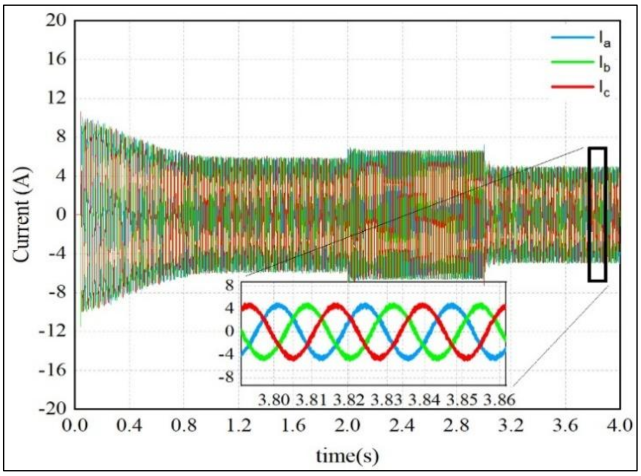

Figure 7: Line currents.
Source: Authors, (2026).

In Figure 6, the squirrel-cage induction motor is supplied with voltages stable and close to their nominal values. A small, correlated variation in terminal voltage is observed with the changing in irradiance, increasing slightly during high-irradiance periods and decreasing when irradiance drops. According to Figure 7, the transient regimes of the motor are relatively insignificant, where the current demand during the transient regime is approximately 1.5 times higher than that in the nominal regime. The proposed control strategy enables a gradual start-up of the load to ensure a current demand lower than that of the short-circuit of the PV generator.

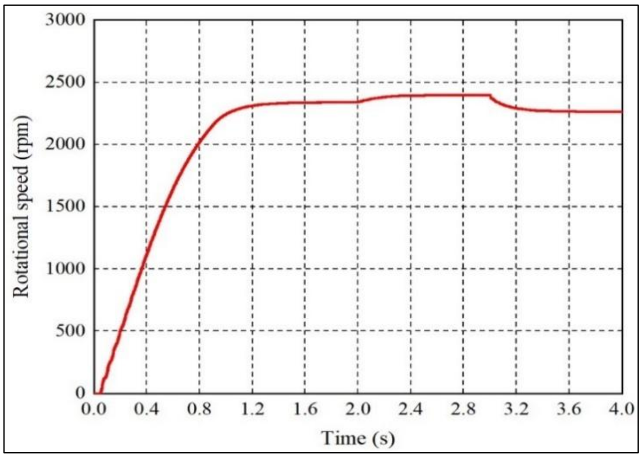

Figure 8: Rotational speed.
Source: Authors, (2026).

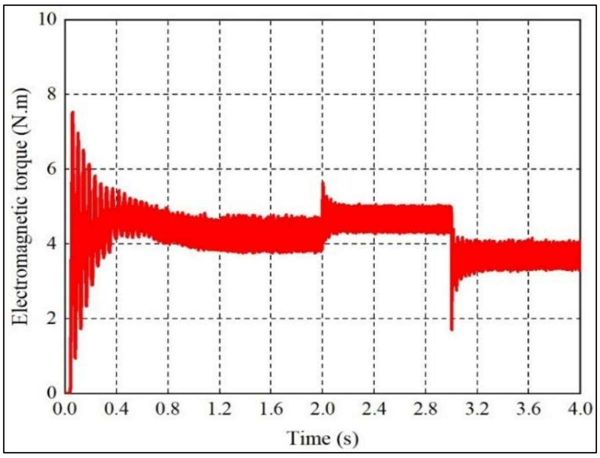

Figure 9: Electromagnetic torque.
Source: Authors, (2026).

From Figure 8, the motor requires approximately 1.2 seconds from startup to reach its nominal rotational speed. This period is characterized by transient oscillations in the electromagnetic torque (Figure 9).The system demonstrates effective load adaptation. A decrease in irradiance causes a corresponding decrease in both electromagnetic torque and rotational speed, shifting the operating point to match the available power from the PV generator. Conversely, an increase in irradiance allows the motor to accelerate to a higher speed, increasing both torque and rotational speed. The consistent variance between electromagnetic and load torque (Figure 10) is attributed to viscous friction losses within the motor.

The pump begins discharging water only after reaching a threshold speed of 2154 rpm. A delay of approximately 0.8 s is observed before water flow begins (Figure 11), corresponding to the time required to fill the hydraulic circuit and for the total head (Figure 12) to overcome the combined static head and dynamic head losses of the circuit. From Figure 11, the water flow rate is directly governed by the motor speed, which is itself dependent on irradiance. During irradiance decrease, a significant drop in flow rate is observed as the motor speed decreases. Form Figure 12, the total head, being a function of the flow rate, decrease proportionally during low-flow periods and increase again during high-flow periods.

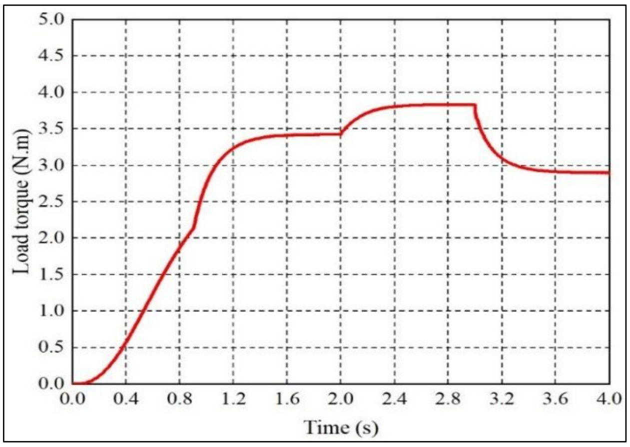

Figure 10: Load torque.
Source: Authors, (2026).

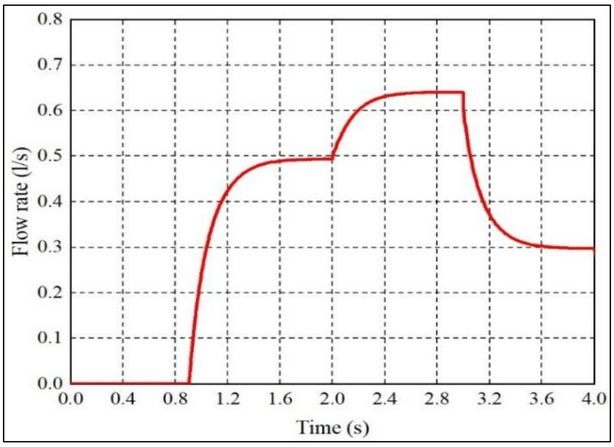

Figure 11: Flow rate.
Source: Authors, (2026).

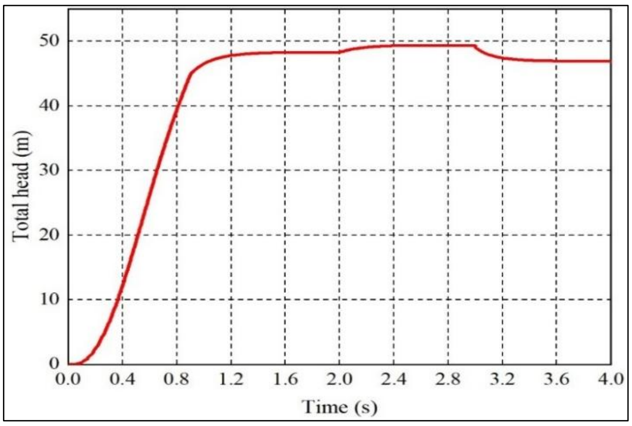

Figure 12: Total head.
Source: Authors, (2026).

IV. CONCLUSIONS

This study presents a dynamic simulation of a standalone solar water pumping system to evaluate performance under varying irradiance. Four machine-learning techniques (ANN, ANFIS, SVM, and GPR) were compared for predicting the MPP voltage of the PV generator. The results show that ANFIS delivers superior accuracy ($R^2 = 0.9992$ and RMSE = 0.9552) and was therefore integrated into the PVWPS control strategy. A robustness test involving sudden changes in irradiance demonstrated that the ANFIS-based MPPT maintains the PV voltage close to its optimal value with rapid response, confirming its suitability for solar water pumping applications. In conclusion, the system successfully tracks irradiance variations, dynamically adjusting the motor speed and pump flow rate to the available solar power, ensuring smooth motor transients, and enabling efficient hydraulic output across multiple steps of increasing and decreasing irradiance.

V. AUTHOR’S CONTRIBUTION

Conceptualization: Islam Hachemi, Kamel Haddouche, Ahmed Bouzidane and Mustapha Belarbi.
Methodology: Islam Hachemi and Kamel Haddouche.
Investigation: Islam Hachemi, Kamel Haddouche, Ahmed Bouzidane and Mustapha Belarbi.
Discussion of results: Islam Hachemi, Kamel Haddouche, Ahmed Bouzidane and Mustapha Belarbi.
Writing – Original Draft: Islam Hachemi and Kamel Haddouche.
Writing – Review and Editing: Islam Hachemi and Kamel Haddouche.
Resources: Islam Hachemi and Kamel Haddouche.
Supervision: Islam Hachemi and Kamel Haddouche.
Approval of the final text: Islam Hachemi, Kamel Haddouche, Ahmed Bouzidane and Mustapha Belarbi.

VI. REFERENCES

[1] T. Chen, A. Harrison, N. H. Alombah, M. Aurangzeb, S. Iqbal, and H. A. Mahmoud, “A simplified control algorithm for efficient and robust tracking of the maximum power point in PV systems,” Control Engineering Practice, vol. 148, p. 105945, Jul. 2024, doi: 10.1016/j.conengprac.2024.105945.

[2] H. Pallathadka, E. H. Ramirez-Asis, T. P. Loli-Poma, K. Kaliyaperumal, R. J. M. Ventayen, and M. Naved, “Applications of artificial intelligence in business management, e-commerce and finance,” Materials Today: Proceedings, vol. 80, pp. 2610–2613, Jan. 2023, doi: 10.1016/j.matpr.2021.06.419.

[3] R. Sarkar, J. R. Kumar, R. Sridhar, and S. Vidyasagar, “A New Hybrid BAT-ANFIS-Based Power Tracking Technique for Partial Shaded Photovoltaic Systems,” Int. J. Fuzzy Syst., vol. 23, no. 5, pp. 1313–1325, Jul. 2021, doi: 10.1007/s40815-020-01037-y.

[4] N. Pachaivannan, R. Subburam, M. Padmanaban, and A. Subramanian, “Certain investigations of ANFIS assisted CPHO algorithm tuned MPPT controller for PV arrays under partial shading conditions,” J Ambient Intell Human Comput, vol. 12, no. 10, pp. 9923–9938, Oct. 2021, doi: 10.1007/s12652-020-02738-w.

[5] R. De Leone, M. Pietrini, and A. Giovannelli, “Photovoltaic energy production forecast using support vector regression,” Neural Comput & Applic, vol. 26, no. 8, pp. 1955–1962, Nov. 2015, doi: 10.1007/s00521-015-1842-y.

[6] R. Nageem and J. R, “Predicting the Power Output of a Grid-Connected Solar Panel Using Multi-Input Support Vector Regression,” Procedia Computer Science, vol. 115, pp. 723–730, Jan. 2017, doi: 10.1016/j.procs.2017.09.143.

[7] S. Chandra, P. Gaur, and D. Pathak, “Radial basis function neural network based maximum power point tracking for photovoltaic brushless DC motor connected water pumping system,” Computers & Electrical Engineering, vol. 86, p. 106730, Sep. 2020, doi: 10.1016/j.compeleceng.2020.106730.

[8] M. M. Ahmed, W. S. Hassanien, and M. A. Enany, “Modeling and evaluation of SC MPPT controllers for PVWPS based on DC motor,” Energy Reports, vol. 7, pp. 6044–6053, Nov. 2021, doi: 10.1016/j.egyr.2021.09.055.

[9] S. Djeriou, A. Kheldoun, and A. Mellit, “Efficiency Improvement in Induction Motor-Driven Solar Water Pumping System Using Golden Section Search Algorithm,” Arab J Sci Eng, vol. 43, no. 6, pp. 3199–3211, Jun. 2018, doi: 10.1007/s13369-017-2972-6.

[10] S. Haddad, M. Benghanem, A. Mellit, and K. O. Daffallah, “ANNs-based modeling and prediction of hourly flow rate of a photovoltaic water pumping system: Experimental validation,” Renewable and Sustainable Energy Reviews, vol. 43, pp. 635–643, Mar. 2015, doi: 10.1016/j.rser.2014.11.083.

[11] F. Belhachat and C. Larbes, “Global maximum power point tracking based on ANFIS approach for PV array conFigureurations under partial shading conditions,” Renewable and Sustainable Energy Reviews, vol. 77, pp. 875–889, Sep. 2017, doi: 10.1016/j.rser.2017.02.056.

APPENDIX A

A.1 ANN APPROACH

A standard feed-forward artificial neural network (ANN) was employed. Its architecture consists of input, hidden, and output layers. The hidden layer contains neurons that perform internal processing; the neuron's output (s_j) is calculated as follows:

$$s_j = g\left(\sum_{i=1}^{m} w_{ij} \cdot e_i - b_j\right) \tag{A.1}$$

The weights (w_{ij}) and bias (b_j) are adjustable parameters. Users can select the transfer function, number of hidden layers and neurons, and training algorithm to optimize performance. A linear transfer function was chosen for the output, and a hyperbolic tangent sigmoid one for the hidden layer to obtain better performances. The used training function is the Bayesian Regularization. After the training phase for different numbers of hidden neurons, the best configuration is given for a 2-3-1 structure.

A.2 ANFIS TECHNIQUE

The ANFIS architecture is characterized by five layers. For an ANFIS configured with two inputs, denoted as x_1 and x_2, the output of each layer is determined by the following equations [11]:

$$L_{1,i} = \mu A_i(x_1), \qquad for\ i = 1,2 \ldots j \tag{A.2}$$

$$L_{1,i} = \mu B_i(x_2), \qquad for\ i = 1,2 \ldots j \tag{A.3}$$

$$L_{2,i} = W_i = \mu A_i(x_1) \cdot \mu B_i(x_2), \qquad for\ i = 1,2 \ldots j^2 \tag{A.4}$$

$$L_{3,i} = \overline{W}_i = \frac{W_i}{\sum_{i=1}^{j^2} W_i} \tag{A.5}$$

$$L_{4,i} = \overline{W}_i f_i = \overline{W}_i (p_i x_1 + q_i x_2 + r_i) \tag{A.6}$$

$$L_{5,i} = \sum_{i=1}^{j^2} \overline{W}_i f_i = \frac{\sum_{i=1}^{j^2} W_i f_i}{\sum_{i=1}^{j^2} W_i} \tag{A.7}$$

Where μA_i and μB_i are the membership functions and (p_i, q_i, r_i) are the linear parameters.

A.3 GPR MODEL

Given a training dataset of input (x_i) and target (y_i) values, the relationship between them can be modeled as follows:

$$y_i = f(x_i) + \zeta_i \tag{A.8}$$

The model includes additive Gaussian noise with a mean of zero and variance. In a distributed Gaussian process, $f(x_i)$ can be represented as:

$$f(x_i) \approx GP(m(x_i), K(\mathrm{X}, \mathrm{X}')) \tag{A.9}$$

Where K(X, X') represents the covariance matrix, and $m(x_i) = E[f(x_i)]$ is the expectation function for input x_i.

A.4 SVM MODEL

The learned parameters of the SVM regression, comprising coefficients α_i, support vectors X_i, and bias term b, are extracted to formulate the predictive regression function done by:

$$f(x) = \sum_{i=1}^{n} \alpha_i K(X_i, x) + b \tag{A.10}$$

For the present study, the SVM model was trained by an RBF kernel function given by:

$$K(x_i, x_j) = G(x_i, x_j) = \exp\left(-\frac{\left\|x_i - x_j\right\|^2}{2\sigma^2}\right) \tag{A.11}$$

Where (σ^2) is the variance.

APPENDIX B

Table B: The parameters of the investigated PVWPS.

Element	Parameter	Value
PV Generator (at STC)	Module type	KC200GT
	Maximum power	200 W
	Voltage at MPP	26.3 V
	Current at MPP	7.61 A
	Short-circuit current	8.21 A
	Open circuit voltage	32.9 V
	Temperature coefficient of Isc	3.18×10^{-3} A/°C
	Number of cells	54 per module
	Module's configuration	14 in series
Squirrel-cage motor and centrifugal pump	Nominal power	2200 W
	Nominal speed	2900 rpm
	Nominal line-to-line voltage	380 V
	Nominal frequency	50 Hz
	Stator winding resistance	6.18 Ω
	Stator inductance	0.688 H
	Mutual inductance	0.678 H
	Rotor winding resistance	4.38 Ω
	Rotor inductance	0.688 H
	Pole pair	1
	Rotor inertia moment	0.012 kg·m^2
	Viscous torque constant	0.0033 N·m·s
	Pump coefficients: h_0, h_1, h_2, c_0, c_1, c_2	74.9; 3.559; -5.594; 1.957; 3.476; -0.6107
Hydraulic circuit	Static head	45 m
	Length of pipe	47 m
	Inside pipe diameter	0.04 m
	Pipe wall roughness	0.15 mm
	Computed friction factor	0.0502
	Total fitting loss coefficient	13.5
	Specific drawdown	-1.67 m/(m^3/h)

Source: Authors, (2026).